Computational Investigation of Acoustics and Instabilities in a Longitudinal-Mode Rocket Combustor

R. Smith,* M. Ellis,† G. Xia,‡ V. Sankaran,§ W. Anderson,¶ and C. L. Merkle**
Purdue University, West Lafayette, Indiana 47907

A computational fluid dynamics analysis of acoustic modes and instabilities in an experimental longitudinal test chamber is presented. The experimental configuration is a uni-element recessed injector post combined with a variable-length combustion chamber. The computations employ the nonlinear Euler equations with mass and heat addition in the injector and combustion chamber and response functions to represent combustion dynamics. Analytical solutions and experimental comparisons are used to verify and validate the computational model. The results demonstrate the importance of including the full Euler equations for predicting the frequencies and mode shapes in the injector-combustor configuration as well as for representing nonlinear phenomena such as wave steepening and the excitation of higher harmonics. The present approach therefore promises to be a useful platform for testing and calibrating combustion response functions for combustion instability models.

I. Introduction

COMBUSTION instability occurs when the transient energy release from combustion contributes to the growth of one or more of the fundamental acoustic modes in the combustion chamber, leading to sustained high-amplitude pressure oscillations [1–3]. Such acoustic instabilities have plagued many liquid rocket engine development programs [1]. Their impact can range from minor rough burning incidents to highly catastrophic events. The most dominant characteristic of combustion instability is its unpredictability. A given test program can proceed smoothly with no indication of difficulty and then suddenly encounter an instability incident. The incident may be triggered by the scale-up to a new combustor size, a small change in design, or even something as relatively minor as a change in the fuel temperature. Unequivocal means for establishing that a given design will not encounter difficulty do not exist, and the development of new liquid rocket engines requires extensive (and expensive) full-scale testing before a stable design can be established.

The fundamental mechanisms leading to combustion instability in liquid rocket engines are the coupling of the acoustic modes of the combustor with the injector fluid dynamics, involving fuel/oxidizer injection, spray atomization, and droplet vaporization, and the subsequent gas-phase mixing and combustion heat release [2]. Rayleigh's criterion states that pressure oscillations amplify when heat is released near a region of maximum pressure and that they decay when heat is released near a region of minimum pressure [2]. It is evident that a high degree of fidelity is necessary to capture such complex dynamic interactions. Attempts at modeling combustion instability have ranged from acoustic wave solutions to detailed computational fluid dynamics (CFD) solutions [4–16]. Such models have contributed immensely to the understanding of combustion instability in different combustion systems. However, many challenges remain in the development and practical application of

these models to liquid rocket instability prediction and analysis. For one, the rocket environment is considerably harsher than other combustion environments, because it involves very high pressures, cryogenic propellants, complex injector designs, near-stoichiometric fuel-oxidizer ratios, high combustion temperatures, and so on. The utility of CFD to accurately represent multiphase combustion dynamics in such regimes remains limited by the complexity of the physical submodels and the availability of computational resources. Further, there is also a lack of fundamental data necessary to guide the development of the physical models. It is therefore clear that focused experiments and computational studies of different levels of fidelity are required to make progress in this difficult arena and to eventually develop accurate predictive capabilities.

As mentioned, a hierarchy of modeling approaches have been used for combustion instability analysis. At the most basic level are the wave-equation approaches, pioneered by Crocco [4], Zinn [5], Culick [6], and Yang et al. [7]. These methods involve solving the wave equation combined with source terms that account for injector and combustion response mechanisms [8,9]. Although such solutions can provide a great deal of insight into the coupling of combustion heat release with the acoustic modes, they are frequently limited by inherent simplifications and assumptions, such as the omission of entropy waves and the use of idealized boundary conditions. Moreover, the response functions need to be designed and calibrated with the use of high-quality instability data. On the other hand, the most detailed level of modeling involves large eddy simulations of the multiphase turbulent reacting flowfield in the combustor [10–13]. These methods have the advantage that they do not necessarily require response functions to represent the dynamic response; however, given present-day computer limitations, they are practical only for simple configurations and geometries. Moreover, the state of the art for rocket operating conditions is still at the level of obtaining validated solutions for the mean flow, and the application to combustion dynamics is likely to remain an active research area for the foreseeable future.

An intermediate level of modeling involves solving the full system of conservation laws such as the Euler or the Reynolds-averaged Navier–Stokes equations, coupled with appropriate response functions [14–16]. The Euler or Navier–Stokes equations allow the proper representation of the mean reacting flowfield with physically realistic boundary conditions, whereas the response functions enable the capturing of the unsteady dynamics. Such models are well within the reach of current-day computational resources and have the advantage of including all the fundamental wave phenomena, boundary conditions, and nonlinear effects. As such, they are suitable for use in modern combustor design and instability prediction codes. However, the methods require the specification of

*Graduate Research Assistant. Student Member AIAA.
†Graduate Research Assistant. Student Member AIAA.
‡Postdoctoral Research Fellow. Member AIAA.
§Senior Researcher, Chaffee Hall, 500 Allison Road. Member AIAA.
¶Professor. Member AIAA.
**Vincent P. Riley Professor of Engineering. Member AIAA.

appropriate response functions to model the combustor dynamics, which remains a major limitation. As indicated earlier, combined experimental and computational studies are necessary to help develop and define appropriate forms of response functions. Our modeling approach follows this intermediate level and is closely integrated with two experimental studies, one involving longitudinal modes [17,18] and the second involving transverse modes [19]. The present paper is focused on the computational part of the longitudinal-mode rocket combustor studies.

The objective of the present studies is to establish a well-validated computational model to facilitate the design, development, calibration, and testing of combustor response functions. Because the current focus is on longitudinal modes, the quasi-one-dimensional Euler equations are used as the computational model, which enables broad parametric surveys to be carried out in an efficient manner. The validation studies are performed using linear and nonlinear forcing of the chamber flowfield to obtain the acoustics and instability characteristics of the combustor. The experimental rocket chamber is fed by a uni-element swirl coaxial injector, which is capable of driving spontaneously unstable longitudinal modes in the cylindrical chamber [17,18,20]. The combustor acoustics can be varied by adjusting the length of the combustion chamber, and a range of different modes can be excited in this manner. The main diagnostics available are the pressure time histories at different axial locations on the wall of the combustion chamber, from which resonant frequencies and mode shapes can be discerned. In addition to the validation studies of the experimental tests, preliminary response function results are also presented to demonstrate how the experimental data may be employed to aid in their selection.

The paper is organized as follows. We first present a brief description of the experimental configuration and sample results. This is followed by a description of the computational model and verification studies using analytical solutions of acoustics in a straight duct. Computational results for the experimental longitudinal chamber are then presented, including linear forcing, nonlinear forcing, and response function results. In the final section, we conclude with a summary and a discussion of future research work.

II. Longitudinal-Mode Rocket Combustor

A. Experimental Configuration

A uni-element experiment using a swirl coaxial injector element has been developed to investigate its stability in a longitudinal chamber arrangement [17,18]. Figure 1 shows a schematic of the recessed element. The experiment was designed to spontaneously excite longitudinal instability modes by matching the first longitudinal mode (1L) of the injector tube (or the injector post) with the second longitudinal mode (2L) of the combustion chamber. This creates a pressure antinode at the injector exit that, depending on the magnitude and frequency of oscillation, could potentially couple

with the combustion process, resulting in instability. The injector element itself was sized to replicate the geometry and nominal flow rates of a full-scale oxidizer-rich staged-combustion-cycle injector. As seen in Fig. 1, the oxidizer was fed radially in the injector tube halfway down its length. This creates a fully reflective solid wall boundary; consequently, a pressure antinode forms at the head end of the tube. In addition, the introduction of the oxidizer at a pressure node (assuming that a 1L mode is present) minimizes the chances of impacting the oscillating pressure in the tube. The oxidizer orifices were sized so that a sonic condition was created across them, which acoustically isolates the oxidizer manifold from the oxidizer tube. Two different fuel injectors have been used: a baseline injector that has two rows of four tangential orifices with a pressure drop of 227 kPa, and a second injector with one row of four similar-sized orifices and a pressure drop of about 875 kPa. The chamber pressure was nominally around 2 MPa. Also, the combustion chamber was fitted with a short nozzle to encourage reflection of pressure waves in the combustion chamber.

A schematic of the entire injector and combustor configuration is shown in Fig. 2. Hot oxygen-rich gas was produced by flowing 90% by weight hydrogen peroxide (H_2O_2) through a catalyst bed. The resulting hot gas was at a temperature of approximately 1030 K and was composed of about 42% oxygen and 58% water vapor (by weight). At this temperature, the gas is hot enough to autoignite the kerosene-based JP-8 fuel. The experiment was run at a nominal mixture ratio (O/F) of about 6.3 and a nominal chamber pressure of approximately 2.2 MPa. To systematically investigate the stability rating of the injector element over different acoustic frequencies, the length of the combustion chamber was varied discretely from 10 to 35 in. in 5-in. increments, with 25 in. being the chamber length at which the injector 1L matches the chamber 2L mode. High-frequency pressure measurements were made in the oxidizer and fuel manifolds, the head end of the oxidizer post, and at five different axial locations in the combustion chamber depending on chamber length, as shown in Fig. 2. Additional details of the experimental setup are given in [17,18].

B. Experimental Results

A summary of the measured test data is shown in Table 1. In the test case column, the first two numbers indicate the length of the combustion chamber in inches, the letter indicates the fuel flow rate (where D is the design, H is the high flow, and L is the low flow), the last number indicates the injector used (where 1 is a low-pressure drop and 2 is a high-pressure drop), and r stands for a repeated test. Therefore, a test designated 25D1 indicates the combustor was run with a 25-in. chamber, the low pressure drop injector, and at the design fuel flow rate. The majority of the tests are at the design fuel flow rate of 0.073 kg/s with the low pressure drop injector. As seen in Table 1, high-amplitude spontaneously excited combustion instabilities were observed in all but one test (corresponding to the
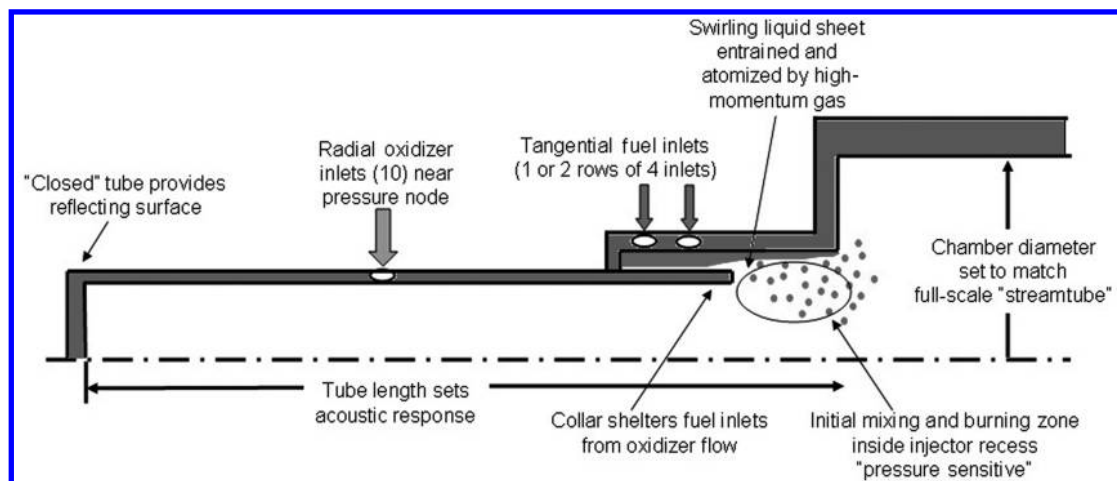

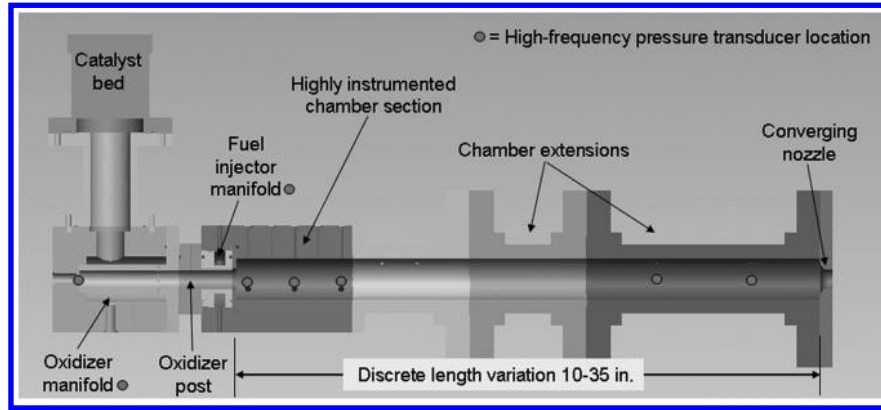Fig. 1   Schematic of oxidizer-rich staged combustor main chamber element.

Fig. 2 Longitudinal chamber configuration showing oxidizer and fuel manifolds, injector post, combustion chamber, and nozzle. Small circles indicate the locations of the high-frequency pressure transducers.

10-in. chamber length). In general, unstable combustion occurred within an unstable frequency bandwidth from 1100 to 1800 Hz. In all cases, limit cycle amplitudes were obtained, and the last column gives the magnitudes of the fluctuating pressure. Finally, we note that repeated cases showed good agreement, indicating that the unstable cases were consistently repeatable.

The time histories of the pressure were obtained at several locations along the combustion chamber and in the oxidizer and fuel manifolds, as shown in Fig. 2. A typical pressure history for an unstable case (test 25D1r) is given in Fig. 3, in which spontaneous growth of pressure oscillations followed by a high-amplitude limit cycle is shown. The high-frequency pressure measurements can be analyzed to obtain power spectral density (PSD) plots, as shown in Figs. 4a–4f for several combustion chamber lengths. Each of these tests was run at the design fuel flow rate and with the low pressure drop injector, and the PSDs were calculated based on pressure data measured at the 0.5-in. location in the combustion chamber. Multiple unstable peaks were observed in each of the tests, and Table 1 lists the frequency of the highest peak in the PSD plot. In all cases, the unstable frequency corresponds to the first three longitudinal modes of the combustion chamber, and the selection appears to be determined by the mode that lies in the 1100–1800 Hz band. For the 35-in. chamber, the unstable frequency was observed to transition from a frequency of about 1720 Hz (approximately equivalent to the chamber 3L mode) to a frequency of 1230 Hz (the chamber 2L mode). This shift in frequency can be seen in the PSD results calculated from the data collected early and late in the test (see Fig. 4e and 4f).

III. Computational Model

A. Mean-Flow Model

The computational model for the longitudinal chamber setup uses the quasi-one-dimensional unsteady Euler equations for multiple species:

$$\frac{\partial Q}{\partial t} + \frac{\partial E}{\partial x} = H + H_f + H_q \tag{1}$$

where

$$Q = \begin{pmatrix} \rho A \\ \rho u A \\ e A \\ \rho Y_{\text{Ox}} A \end{pmatrix} \qquad E = \begin{pmatrix} \rho u A \\ (\rho u^2 + p)A \\ (e + p)u A \\ \rho u Y_{\text{Ox}} A \end{pmatrix} \qquad H = \begin{pmatrix} 0 \\ p\frac{dA}{dx} \\ 0 \\ 0 \end{pmatrix}$$

where x and t are the space and time variables, ρ is the density, u is the velocity, e is the total energy, p is the pressure, Y_{Ox} is the mass fraction of the oxidizer, and $A = A(x)$ is the area of the duct. We note that the quasi-one-dimensional formulation allows the injector post, combustion chamber, and exit nozzle (see Fig. 2) to be combined within a single computational domain with no special treatments at the interfaces between these zones. The oxidizer and fuel manifolds are not included in the computational domain and the oxidizer and fuel flow rates are specified as boundary conditions and source terms, as will be discussed.

This system of equations is written for a multicomponent and/or multiphase homogeneous mixture [21]. The two species considered here are the oxidizer and combustion products. The mass fraction of the combustion products is given by

$$Y_{\text{Pr}} = 1 - Y_{\text{Ox}} \tag{2}$$

The combustion of the oxidizer with the fuel results in the formation of the products of combustion. The addition of the fuel and the subsequent depletion of the oxidizer are modeled through source terms, as will be discussed.

The second source term in Eq. (1), H_f, represents the addition of the fuel and its combustion with the oxidizer, which in turn results in the formation of the combustion products. A single-step reaction-progress variable is used to represent the heat release and fluid property changes associated with the combustion. Note that the
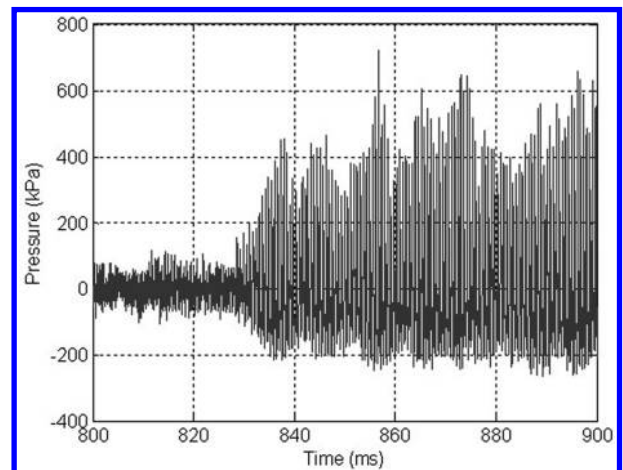
Table 1 Test conditions for the longitudinal chamber experiments

Test case	L_c, in.	O/F	η_{c^*}	P_c, MPa	Unstable freq., Hz	P', kPa
10D1	10	6.4	94.2	2.4	Stable	13.8
15D1	15	6.4	87.4	2.2	1502	297
20D1	20	6.6	86.3	2.2	1184	152
20D1r	20	6.4	90.1	2.3	1184	166
25H1	25	5.3	83.4	2.2	1672	434
25L2	25	8.0	88.4	2.2	1648	159
25D1	25	6.6	83.8	2.1	1709	331
25D1r	25	6.3	87.3	2.2	1660	255
25D2	25	6.4	86.5	2.2	1672	269
35D1 early	35	6.4	86.0	2.2	1721	241
35D1 late	35	6.4	87.7	2.2	1233	145

Fig. 3 Pressure time history for a typical unstable chamber test.
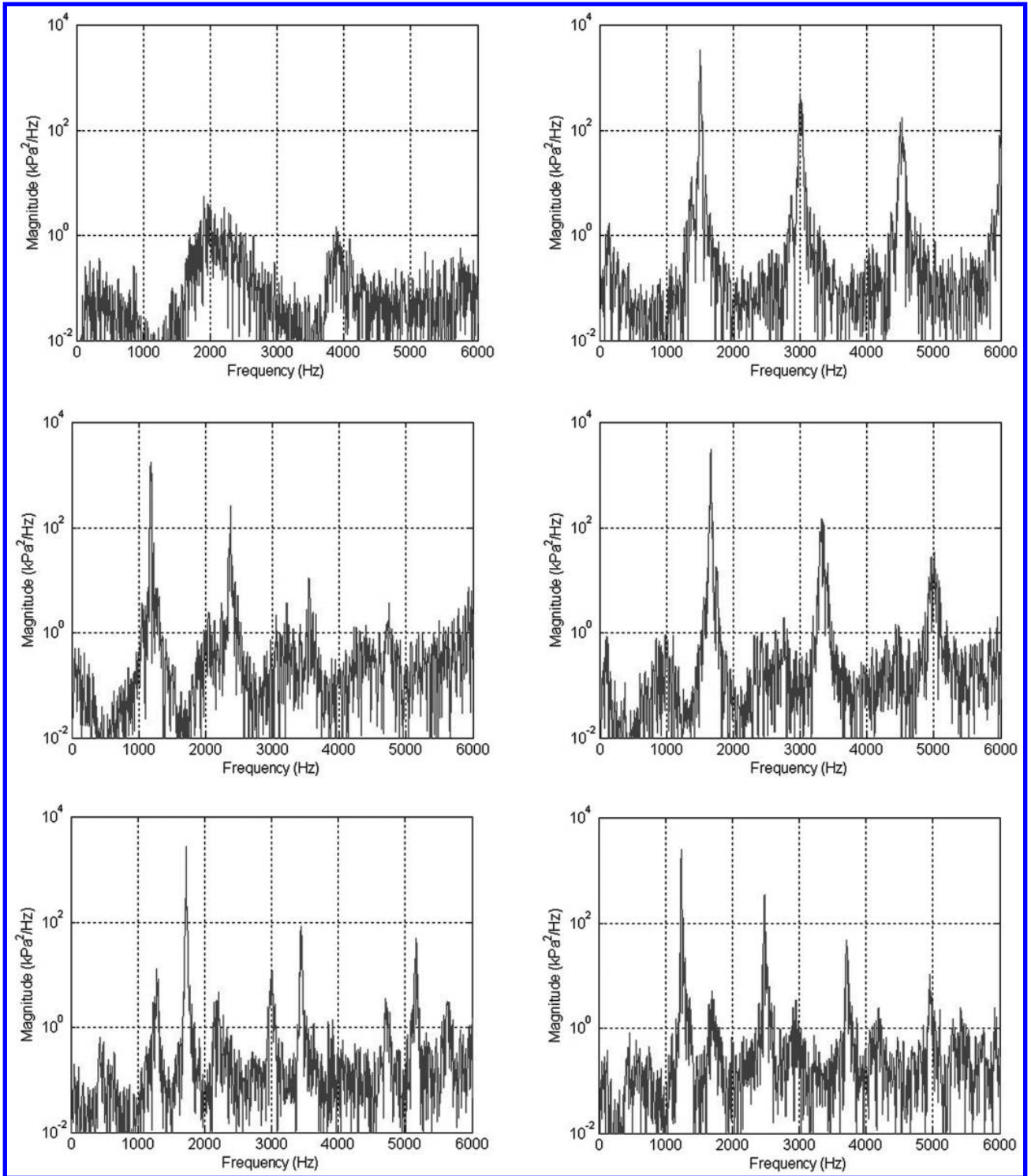
Fig. 4   Power spectral density plots from tests: a) 10D1, b) 15D1, c) 20D1r, d) 25D1r, e) early in 35D1, and f) late in 35D1.

properties of the combustion products are established by using appropriate equilibrium mixture properties, determined by using the chemical equilibrium with applications (CEA) equilibrium code [22]. The corresponding source-term vector is

$$H_f = \begin{pmatrix} \dot{w}_f \\ \dot{w}_f u \\ \dot{w}_f h_o \\ -\dot{w}_{Ox} \end{pmatrix} \qquad (3)$$

Here, the first three terms represent the addition of the fuel, whereas the last term represents the chemical reaction of the oxidizer with the fuel. We note that the fuel mass fraction is not explicitly solved for in

our model. Rather, we specify the depletion of the oxidizer using an assumed "combustion" profile. Then, fuel is added in proportion to the depleted oxidizer and the mixture is assumed to be converted instantly into combustion products.

The specific definitions of the mass transfer terms used in the present study are

$$\dot{w}_f = C_{f/o}\dot{w}_{Ox} \qquad (4)$$

$$\dot{w}_{Ox} = k_f \rho Y_{Ox}(1 + \sin \xi) \qquad (5)$$

where $C_{f/o}$ is the fuel-to-oxidizer ratio. The second equation concerns the rate of depletion of the oxidizer, and k_f is a reaction constant. The term ξ specifies the extent of the assumed combustion zone and is given by

$$\xi = -(\pi/2) + ((x - l_s)/(l_f - l_s))2\pi \quad \forall \ l_s < x < l_f \quad (6)$$

where l_s and l_f are the axial locations of the beginning and end of the combustion zone. The reaction constant k_f is selected so as to insure that the oxidizer is consumed within the specified combustion zone. The selection of l_s, l_f, and k_f are obtained by trial and error and designed to approximately match the mean conditions in the combustion chamber [23]. The specific values used in the current study are: $l_s = 0$ in., $l_f = 10$ in., and $k_f = 2000/s$. In other words, the combustion is taken to initiate immediately downstream of the injector face and to cease at a distance of 10 in. from the injector face. For the choice of parameters given, the combustion is completed well within the 10-in. interval for all the test cases. Indeed, this result is supported by the fact that the measured combustion efficiencies are relatively independent of the chamber length (see Table 1).

The enthalpy of the oxidizer and products of combustion are given as

$$h_{Ox} = h_{f,Ox} + C_{p,Ox}(T - T_r) \quad (7)$$

$$h_{Pr} = h_{f,Pr} + C_{p,Pr}(T - T_r) \quad (8)$$

where h_f is the heat of formation, C_p is the specific heat, T is the local temperature, and T_r is a reference temperature. We arbitrarily set the heat of formation of the oxidizer to be zero and the heat of formation of the products to be equal to the combustion heat release. The mixture enthalpy is given by

$$h = h_{Ox}Y_{Ox} + h_{Pr}Y_{Pr} \quad (9)$$

For the present application, the heat of formation of the products was set to $5.15e6$ J/kg, that corresponded to a flame temperature of about 2700 K and that in turn was in good agreement with the CEA results [22].

Boundary conditions for the longitudinal chamber include inflow conditions at the head end of the injector and supersonic outflow at the exit of the converging–diverging nozzle (downstream of the combustion chamber). We note that, in the experiments, the oxidizer is introduced radially near the midpoint location of the injector post (see Fig. 1). In the present quasi-one-dimensional model, it is not possible to introduce the oxidizer radially. Therefore, the oxidizer is introduced axially through the head end of the oxidizer post and a fixed mass flow boundary condition is enforced here, which is acoustically similar to a closed-end boundary condition. Limited experimental testing conducted recently with an axial-inflow injector has indicated that the experimental results are relatively insensitive to the mode of oxidizer injection in the oxidizer post.[††] Moreover, as shown later, the computational predictions from the present model demonstrate excellent agreement with the experimental estimates of the acoustic mode shape in the injector post and chamber, thereby justifying the choice of boundary condition as well as the aforementioned overall mean-flow model.

B. Linear and Nonlinear Forcing

Combustion instability is caused by the interaction of the acoustics field with the multiphase turbulent reacting flow dynamics of the injector flowfield. Detailed modeling of these effects require significant computational resources and is beyond the scope of the present paper. Accordingly, the computational model is operated in steady-state mode first to obtain the mean-flow solution that is relevant for a given test condition. Following this, the code is run in unsteady mode to obtain the acoustic response. This is accomplished in one of two ways: one, by forcing the inlet oxidizer mass flow and,

two, by introducing a combustion response function in the energy equation. Both options are briefly described herein.

Forcing the oxidizer flow rate is an effective means of determining the acoustic response of the injector-combustor configuration. Previous trials using a random forcing function resulted in noisy data; therefore, we employ a discrete broadband forcing, which modulates the inlet oxidizer mass flux boundary condition:

$$\dot{m}_{Ox}(t) = \dot{m}_{Ox,mean} \sum_{k=1}^{K} [1 + \epsilon \sin 2\pi(f_0 + k\Delta f)t] \quad (10)$$

where f_0 is the minimum frequency, Δf is the frequency interval, and K is the number of discrete modes. Typical values used in our studies are $f_0 = 50$ Hz, $\Delta f = 50$ Hz, and $K = 240$, that is, $f = 50$–6000 Hz at 50 Hz intervals. Smaller frequency steps were also tried, but did not yield substantially different results.

The broadband Fourier forcing is an efficient approach for obtaining a complete frequency spectrum from a single computational run. Typically, we specify a small amplitude of the ϵ parameter to obtain the acoustic response for a given test condition. In addition, small-amplitude single-frequency forcing is also performed to obtain the corresponding mode shapes. Further, large-amplitude single-frequency forcing is used for studying nonlinear effects, such as wave steepening and the excitation of higher harmonic modes. Examples of these computational studies are discussed in Sec. IV.

C. Combustion Response Model

The discrete broadband or single-frequency forcing already mentioned does not include any mechanism for coupling the combustion heat release to the acoustic modes, without which one cannot incite and sustain combustion instability. Explicit mechanisms for such a coupling may be introduced in the form of combustion response functions. However, there is no general theory for the design of such response functions, and the models need to be designed and calibrated to match particular test conditions. In this paper, we consider a simple and preliminary model for combustion response by introducing a fluctuating heat-release term in the third source-term vector in Eq. (1), H_q:

$$H_q = \begin{pmatrix} 0 \\ 0 \\ q''' \\ 0 \end{pmatrix} \quad (11)$$

where the heat-release term is expressed as a function of the instantaneous pressure with a time lag built into the response function [4,9].

$$q'''(x,t) = \bar{Q} \cdot n \cdot \alpha(x) \left(\frac{p(x, t - \tau) - \bar{p}(x)}{\bar{p}(x)} \right) \quad (12)$$

where $\bar{Q}$ is the integral mean combustion heat release and $\alpha(x)$ is a scaling constant that is generally dependent on space, but independent of time. In our calculations, we set the term to be nonzero at the combustion flame front and zero everywhere else:

$$\alpha(x) = \frac{1}{\sigma\sqrt{2\pi}} \exp\left(-\frac{(x-\mu)^2}{2\sigma^2} \right) \quad (13)$$

In the present calculations, the following parameters are used: the normalized interaction index, $n = 2.05$; the phase lag, $\tau = 0$; $\mu = 2$ in.; and $\sigma = 0.5$ in.. Thus, the combustion response is taken to be concentrated at 2 in. downstream of the injector face, which approximately coincides with maximum mean heat-release location. This location is also near the location of a pressure antinode. Therefore, from Rayleigh's criterion, we anticipate that the combustion response term will lead to growth when the heat-release term is in phase with the pressure (i.e., zero time lag). However, we point out that the presence of the inflow and outflow boundary conditions in the chamber introduces additional damping mechanisms, and so we expect that the combustion response

---

[††]J. Sisco, private communication, Purdue University, 2007.

function will lead to instability only for sufficiently large values of the interaction index. The value used here has been established by a trial-and-error process, discussed further in Sec. IV.

We stress here that this simple model is selected only to provide a sample response function for the representative calculations in this paper. Clearly, alternate models for combustion response are possible and many have been proposed in the literature for various combustion systems. However, the purpose of the present paper is the establishment of a validated computational platform that can be used for the development and calibration of appropriate response functions. We therefore focus on the acoustic characterization of the experimental configuration and the validation of the predicted frequencies and mode shapes. The specific development of response functions will be the subject of future research.

D. Numerical Verification

The numerical solutions of the governing equations are carried out using a second-order backward temporal scheme and a second-order flux-difference spatial scheme. Specific details of the numerical algorithm are available elsewhere (for instance, see [21]). Here, we present the verification of the numerical predictions for acoustics in a straight chamber by comparing them with the analytical solutions. The analytical solution procedure is standard and has been used previously for acoustic and instability validation [14]. We therefore do not present the details of the derivation, but note that the analytical solution includes mean-flow effects and generalized boundary conditions. It also has the capability of representing entropy waves and multidimensional modes; however, for simplicity, we restrict the current comparisons to a one-dimensional isentropic flow for different Mach numbers in a straight duct.

For these comparisons, the CFD solution is obtained by starting with a uniform constant-property mean flow in a duct and then modulating the inlet mass flow rate using the discrete broadband forcing described in Eq. (10). The boundary conditions used for these studies correspond to a fixed inlet mass flow rate and a fixed exit pressure. For low Mach numbers, this problem specification is found to be equivalent to a duct with closed-inlet and open-exit conditions. The pressure response is probed at a given axial location in the duct and the Fourier transform is obtained to determine the acoustic response. Figure 5 shows typical results for an 8-in.-long duct at a temperature of 3700 K and a pressure of 64 atm. Results are shown for four different Mach numbers to emphasize the role of including the mean flow in the mode analysis. The resonant frequencies from the CFD model and the analytical solution agree very well: there is little discrepancy at the high Mach numbers, whereas at the low Mach numbers the peak amplitude is not precisely captured. The latter result is due to the use of discrete frequency forcing, and the comparisons improve when the Δf in the frequency band is reduced. Moreover, at the low Mach numbers, we require significantly longer

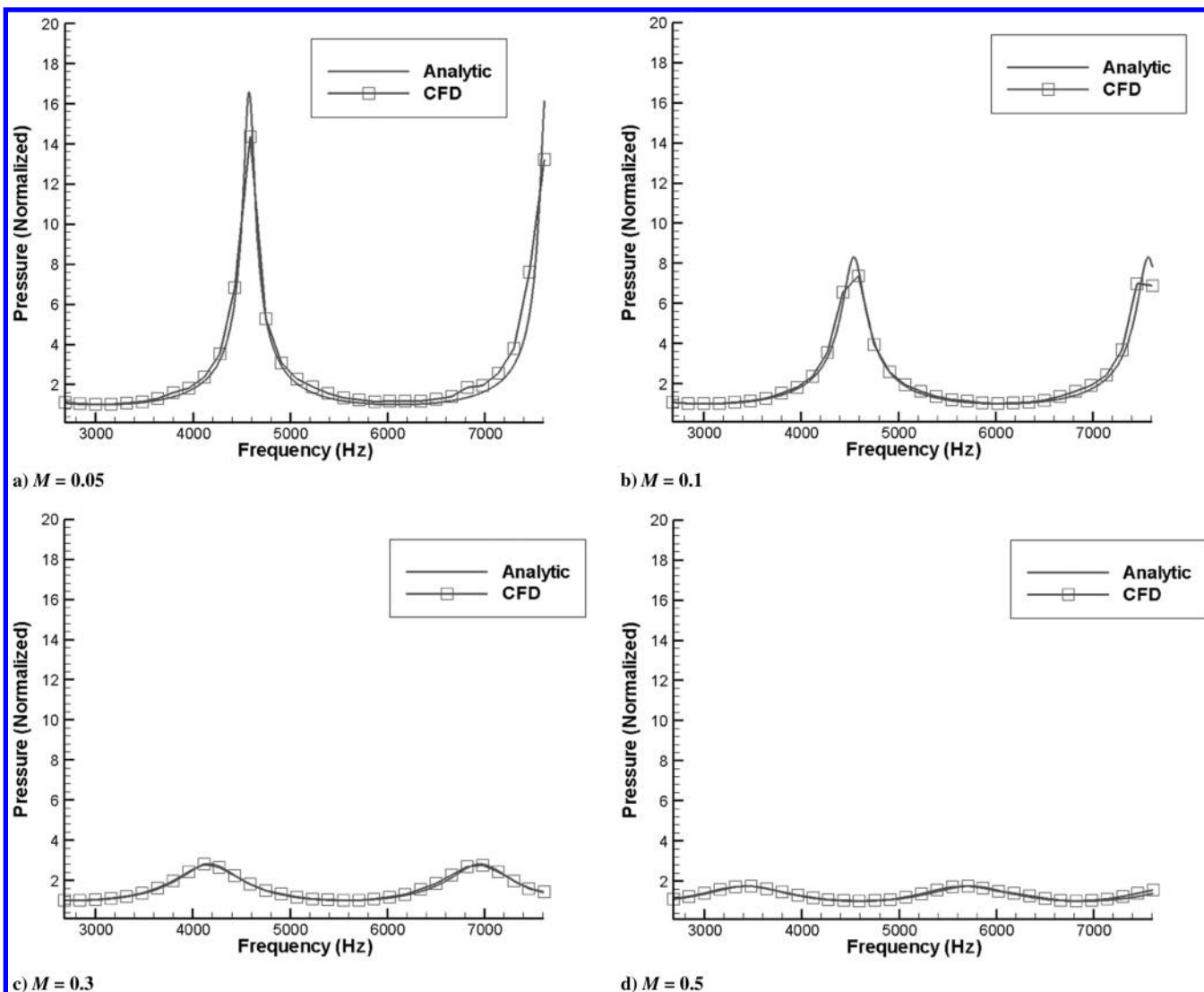a) $M = 0.05$

b) $M = 0.1$

c) $M = 0.3$

d) $M = 0.5$

Fig. 5 Comparison of frequency response with analytical solutions of the linearized Euler equations in a straight duct. Computational results used discrete broadband forcing as given in Eq. (10).

time samples to obtain a converged time response for the problem. This is due to the introduction of entropy waves in the initial condition specification, which have to be subsequently removed from the solution to obtain the requisite "convergence."

For comparison purposes, we show similar results when the inlet mass flow rate is forced using a random forcing function. Figure 6
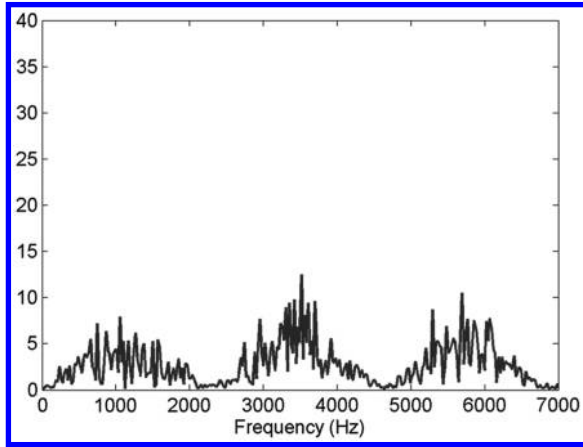
shows the results for a 8-in.-long straight duct with flow at a Mach number of 0.5. Although the trends in the results approximately match the exact frequency response observed in Fig. 5d, the random forcing yields an unacceptably noisy result. For this reason, our studies have employed the discrete forcing described in Eq. (10).

Grid refinement studies have also been carried out for similar straight duct cases. The convergence of the error in the frequency response as a function of the total grid size for two different frequencies is shown in Fig. 7. It can be observed that the slope of the error curve confirms the second-order accuracy of the numerical solution procedure.

Figure 5 also shows the effect of the Mach number on the modal response. It is apparent that, at low Mach numbers, that is, in the absence of mean-flow effects, the resonant frequencies correspond very closely to the classical acoustic modes for a closed-upstream and an open-downstream condition. As the Mach number is raised and mean-flow effects become more significant, the frequency

Fig. 6   FFT results of the head-end pressure for an 8-in. straight duct and flow Mach number of 0.5 with random inlet mass forcing.
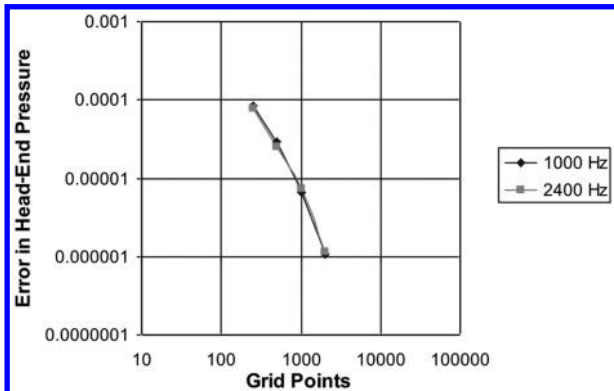
Fig. 7   Grid refinement studies showing error as a function of grid size. Results confirm second-order accuracy of the numerical scheme.
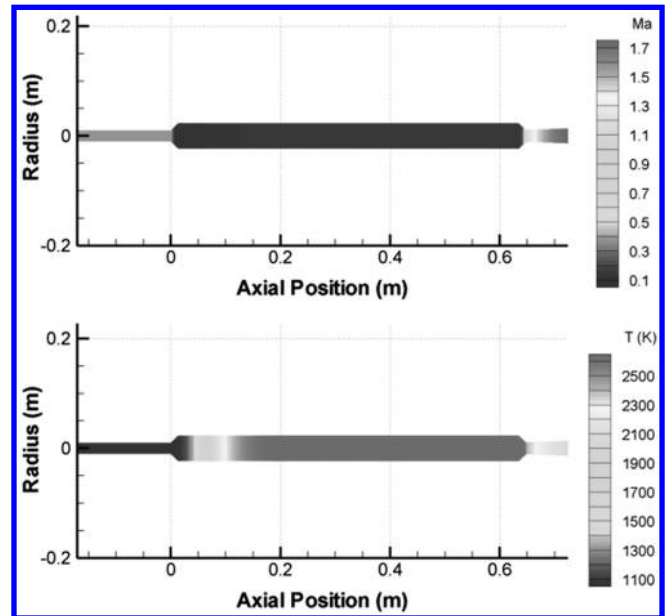

Fig. 9   Longitudinal chamber configuration showing injector post, combustion chamber, and nozzle for a representative case: a) Mach number, and b) temperature contours.
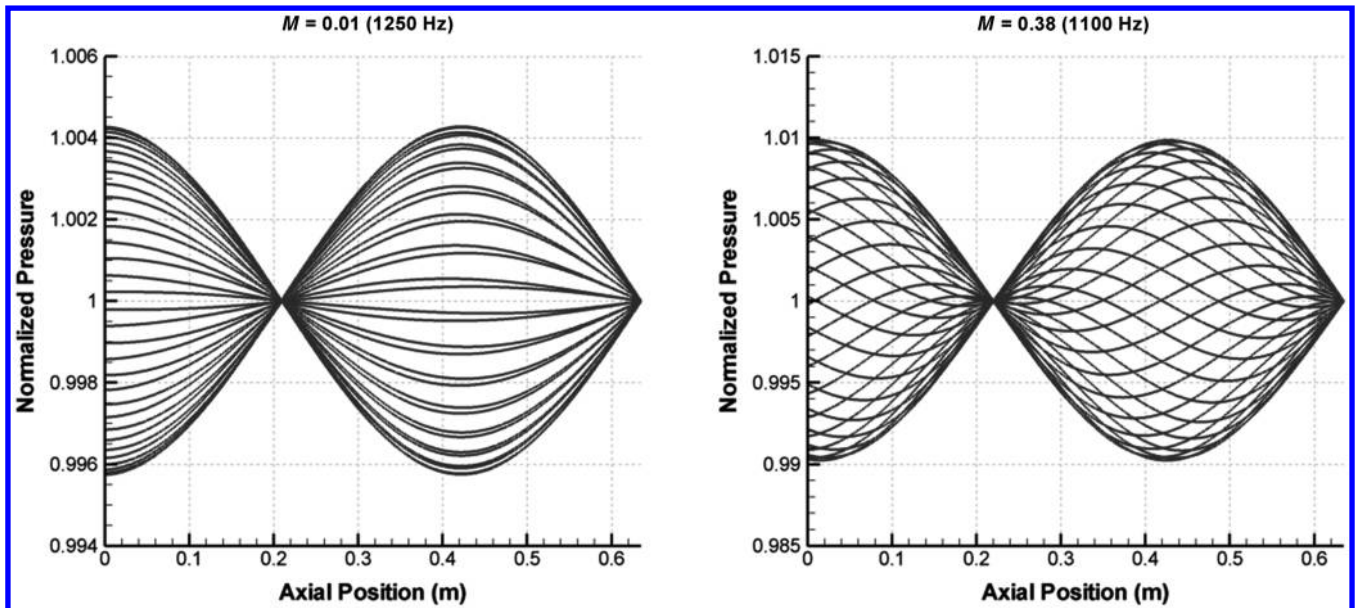

Fig. 8   Mode shapes at low and high Mach numbers for resonant straight duct modes with closed-upstream and open-downstream conditions.

Table 2 Computational conditions used for test 25D1r

Computational conditions	Injector	Chamber
Length, m	0.171	0.635
Cross-sectional area, m²	$3.24e - 4$	$1.64e - 3$
Temperature, K	1010	2700
Pressure, MPa	2.08	2.22
Mass flow rate, kg/s	0.459	0.524

response becomes less sharply centered at a single frequency. Moreover, the resonant frequencies are observed becoming lower in magnitude. It is also interesting to consider the mode shapes at different Mach numbers. To obtain shapes of specific modes, the inlet mass flow is forced at a single resonant frequency. For example, Fig. 8 shows the mode shapes plotted at different instants in time for a single period of oscillation. The results correspond to the second mode of a 25-in. straight duct at two different Mach numbers. As already noted, the higher Mach number case yields a lower resonant frequency (about 10% lower). In addition, the lower Mach number result shows the standing wave oscillating in synchronized fashion in the entire duct, that is, the wave reaches the peak amplitude at all the pressure nodes simultaneously. In contrast, the higher Mach number
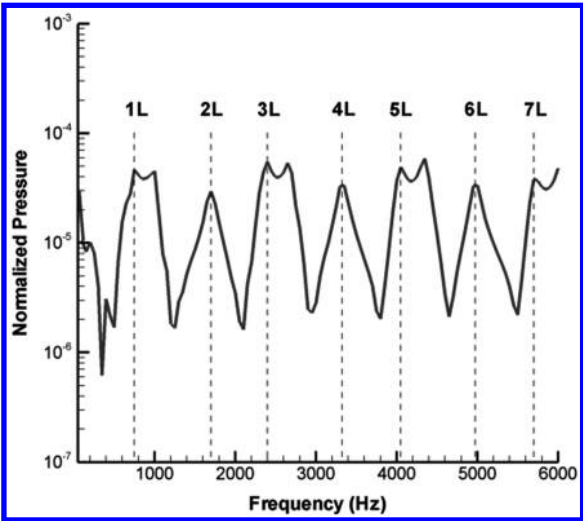

Fig. 10 Computed frequency response for a representative test case (25D1r) with 6.82-in. injector/25-in. chamber.
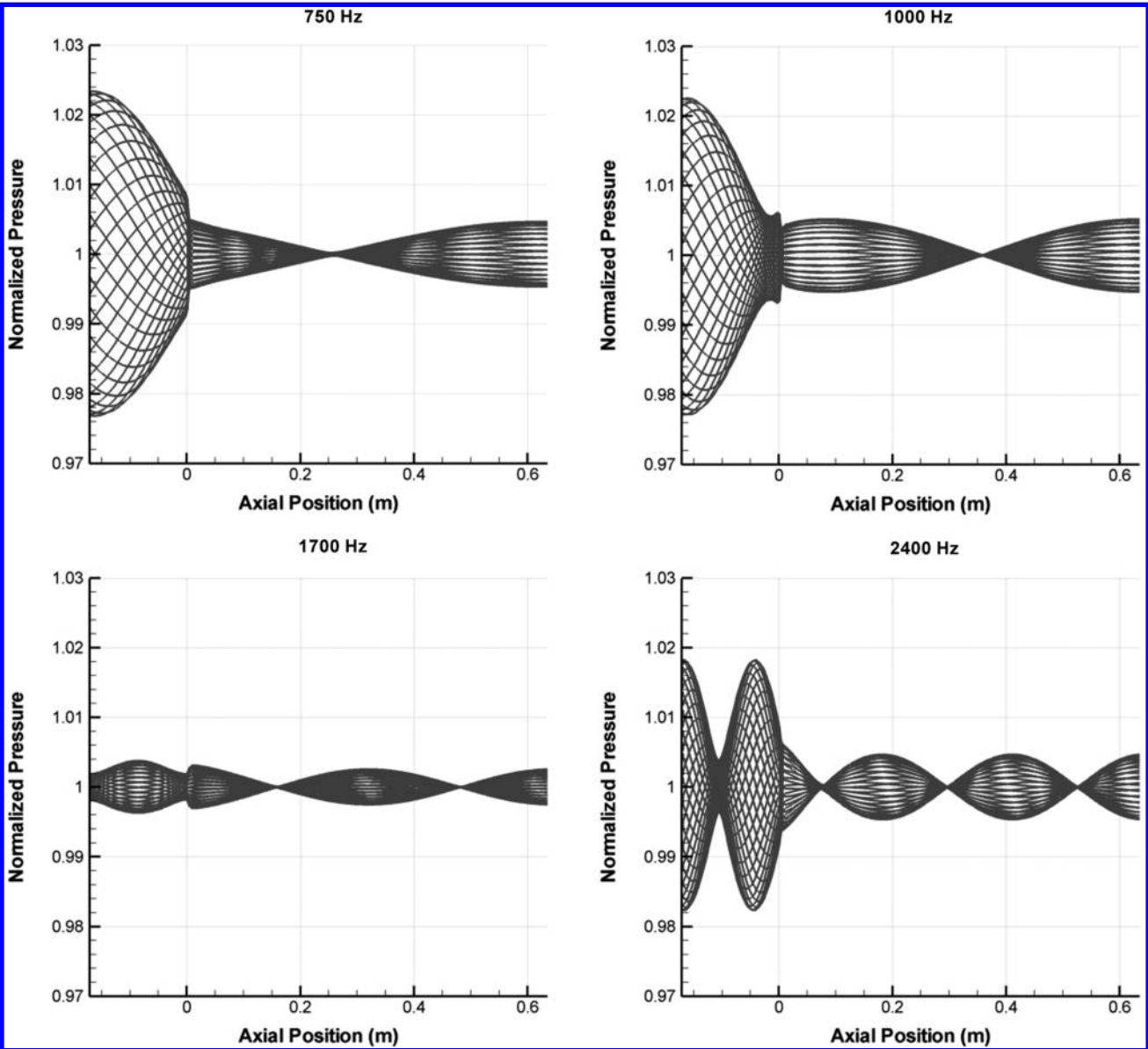

Fig. 11 Computed mode shapes for the first four modes obtained by forcing the chamber at the appropriate mode frequencies. Conditions correspond to test 25D1r.
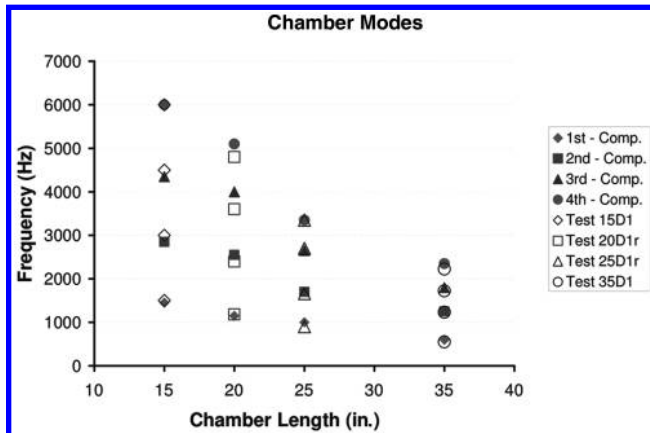
Fig. 12 Comparison of the computed and measured frequencies corresponding to the first four chamber mode frequencies plotted for the 15-, 20-, 25-, and 35-in. chambers. "Comp" refers to the computed data.

case shows a more complex wave shape at any given instant in time, and the pressure reaches the peak at different nodal locations at different instances in time. This inherent phase difference in the wave shape is evidently due to the combined effects of the forward-running $u + c$ and the backward-running $u - c$ waves, which are approximately the same magnitude at low Mach numbers, but have different values at relatively high Mach numbers. Because combustion instability is controlled by the subtle interaction of different physical time scales related to multiphase effects, combustion, turbulence, fluid dynamics, and acoustics, this phase difference is likely to play an important role in the dynamics of real combustion chambers, in which the Mach numbers are typically in the 0.3–0.5 range. It is therefore important that finite Mach number effects are represented correctly in the computational model.

IV. Computational Results

A. Computational Setup

The experimental configuration for the longitudinal-mode chamber shown in Figs. 1 and 2 is modeled using a quasi-one-dimensional geometric representation, as shown in Fig. 9. The upstream narrower section represents the injector oxidizer post, which is followed by the variable-length cylindrical chamber. The injector-chamber flow is choked by a converging–diverging nozzle at the exit end. As noted earlier, oxidizer inflow is specified at the upstream end and the fuel is introduced just downstream of the injector-chamber interface. Pressure time histories are recorded at several axial locations, which include those locations for which experimental data are monitored (as shown in Fig. 2).

Representative test conditions for the experimental test case, test 25D1r, are summarized in Table 2. For this case, the injector is 6.82 in. long and the chamber is 25 in. long. Representative mean-flow solutions for the base case are also shown in Fig. 9. The Mach number and temperature contours are shown. The nominal chamber

pressure is 2.22 MPa. The oxidizer temperature in the injector element is 1010 K and the Mach number is 0.37. The overall $O/F = 6.24$, the chamber combustion temperature is 2700 K, and the chamber Mach number is 0.13. The temperature contours show that, for the model parameters used here, combustion is initiated downstream of the injector face and the mixture is completely burned a short distance thereafter. Similar conditions are employed for the rest of the test cases specified in Table 1.

B. Linear Forcing

As discussed earlier, in the linear forcing studies, the inlet oxidizer mass flow is perturbed using the discrete broadband forcing technique given in Eq. (10). The resulting frequency response for the sample test case, test 25D1r, is shown in Fig. 10. Results are shown for pressure data at the head end of the combustion chamber. Numerous modes are evident at somewhat irregular intervals, which apparently correspond to the superpositioning of the individual chamber and injector modes as well as the bulk (chamber + injector) modes. Superimposed on Fig. 10 are the locations of the first seven pure-chamber modes. These frequency values correspond to the experimental modes seen in Fig. 4; however, there is no preferential selection of the unstable frequencies in the present calculation because no response functions are used. We further note that the experiments indicate an instability at about 1650 Hz, which corresponds to the second chamber mode for these conditions.

A clearer picture of the underlying mode structure emerges when the chamber is forced at individual frequencies and the resulting pressure field is plotted over an entire cycle. Such mode shapes are shown in Fig. 11 for the first four modes for the 251Dr condition. The 750 Hz mode appears to be associated with the first chamber + injector (half-wave) mode, whereas the 1000 Hz appears to be the first chamber (half-wave) mode. The 1700 Hz mode (which is the unstable mode in the experiments) is the second chamber mode. Finally, the fourth mode at 2400 Hz appears to be the third chamber mode.

The experimental results in Fig. 4 clearly reveal the frequency response associated with the various chamber modes. In between the chamber modes, additional modes related to the combined chamber and injector geometry are evident, although the precise frequencies are somewhat difficult to ascertain. To quantitatively compare the measurement data with the predictions for the various test cases, we focus our attention first on the main chamber modes. The corresponding mode frequencies are extracted from the frequency response plots (such as in Fig. 10) for each chamber length and then plotted against the experimental frequencies in Fig. 12. For each chamber length, the first four chamber modes are shown. Excellent quantitative agreement is evident. As expected, the chamber mode frequencies decrease with increasing chamber length, a trend that is captured well by the computational results.

Quantitative comparison of all the modes, that is, the pure-chamber as well as the combined injector-chamber modes, is presented in tabular form for test 25D1r in Table 3. Here, we indicate the intermediate modes in addition to the main chamber modes. The experimental results are extracted from Fig. 4 and are specified as

Table 3   Frequency comparisons for test 25D1r showing results using the classical acoustic model, the present computational model, and the experimental data

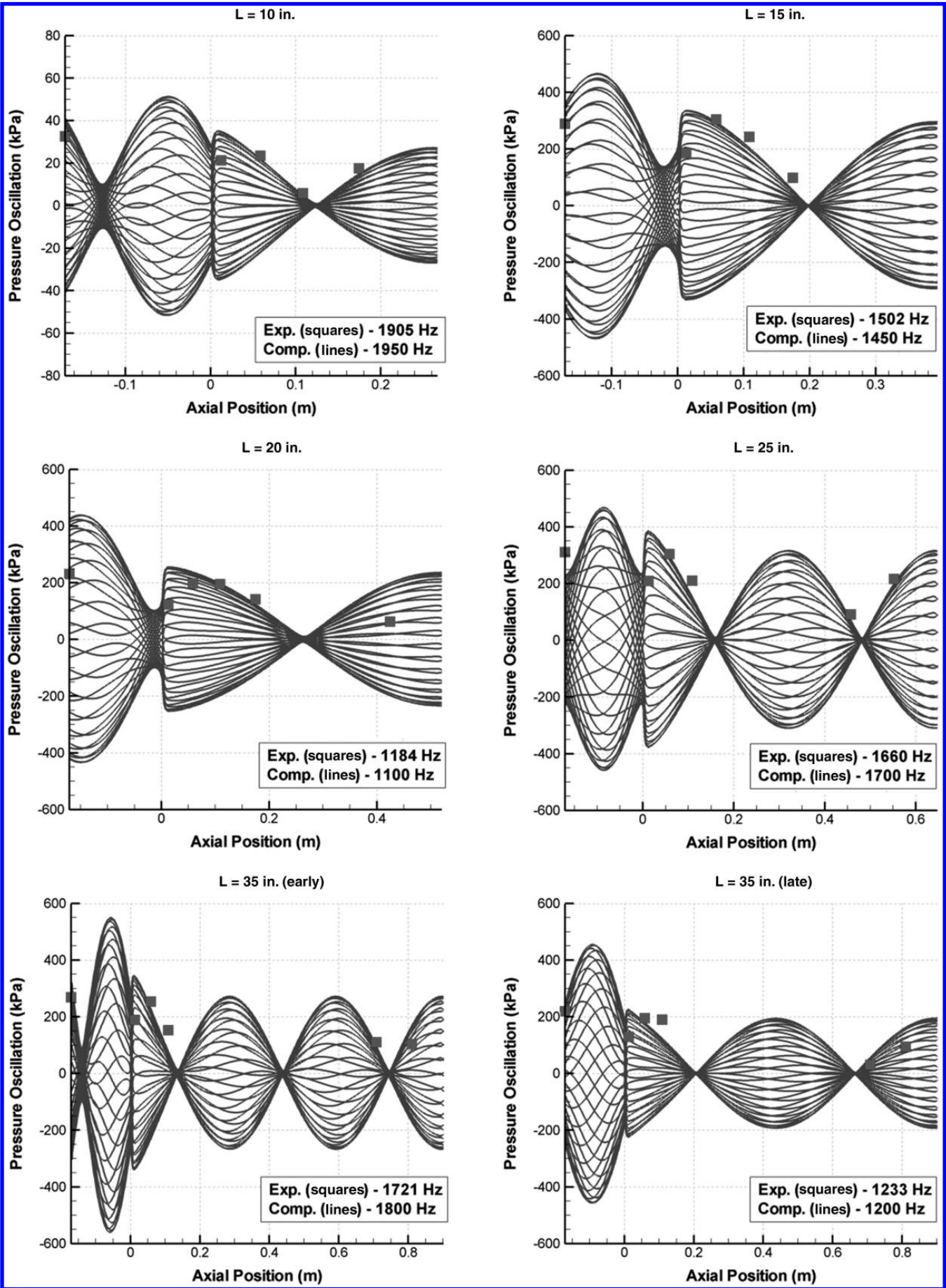| Mode	Acoustic model, Hz	Computational model, Hz	Experimental data, Hz
First chamber	763	750	800–1100
	1055	1000	——
Second chamber	1718	1700	1660
Third chamber	2521	2400	2300–2500
	2946	2650	2600–2800
Fourth chamber	3447	3350	3320
Fifth chamber	4254	4050	4300–4600
	4848	4350	——
Sixth chamber	5190	5000	4956
Seventh chamber	5980	5700	5900

Fig. 13   Comparison of computed and experimentally determined mode shapes for the first three chamber modes for different tests.
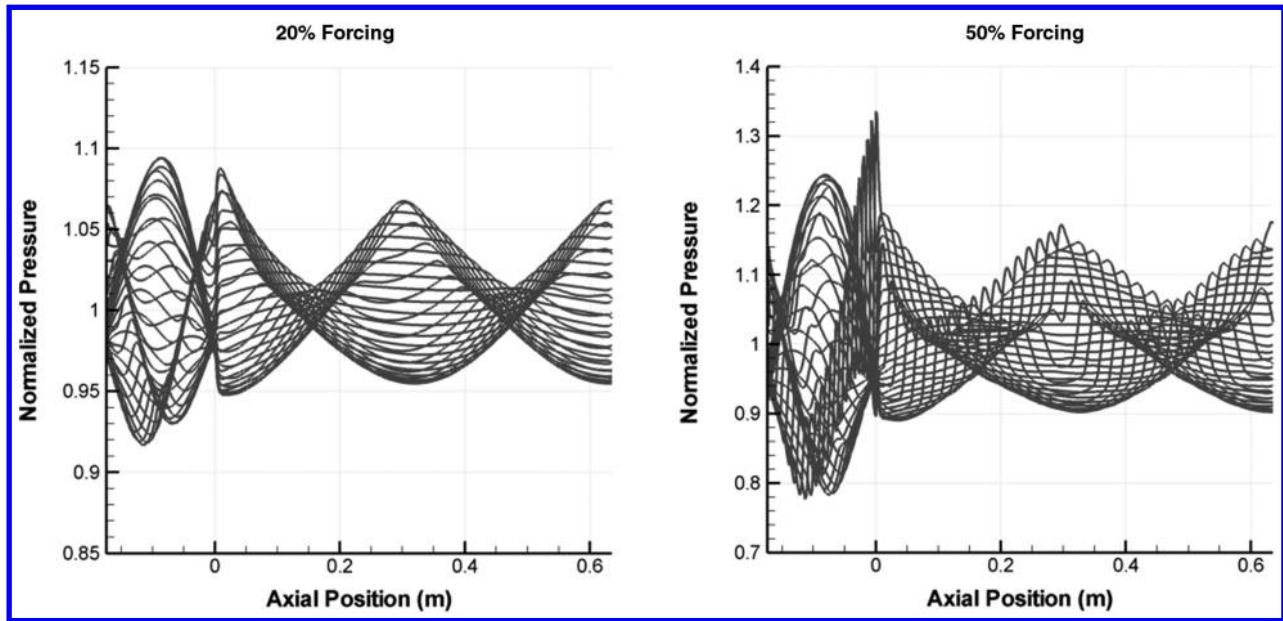
Fig. 14 Computed mode shapes for test 25D1r for high-amplitude forcing of the second chamber mode (1650 Hz).
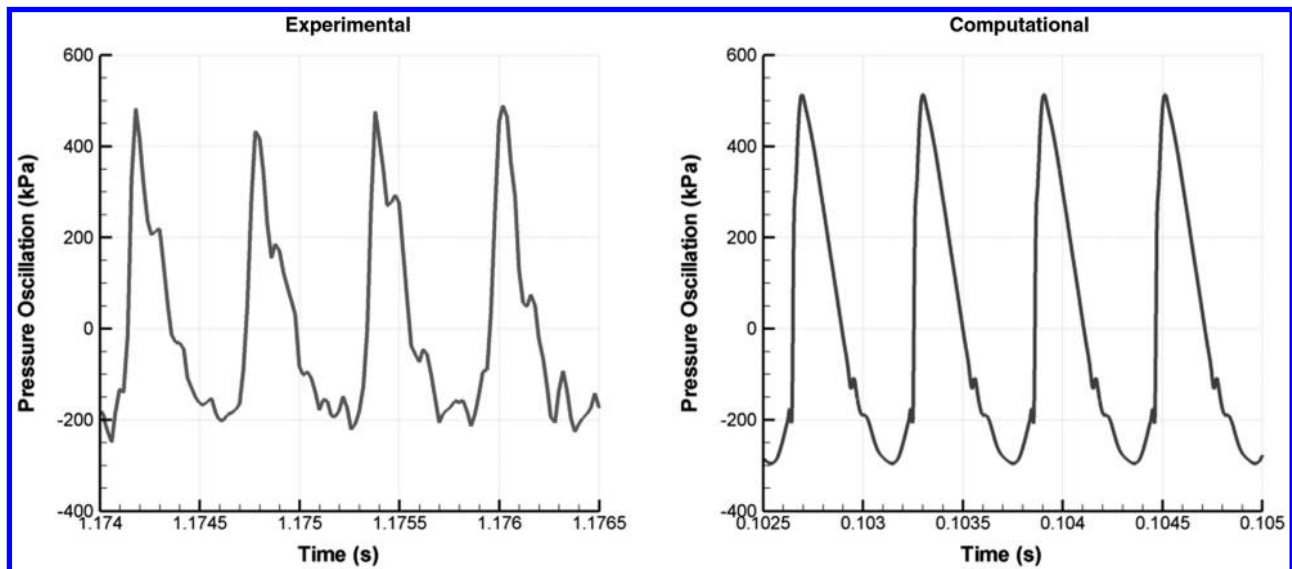

Fig. 15 Pressure time history for high-amplitude computation of the second chamber mode compared with experimental results for test 25D1r.
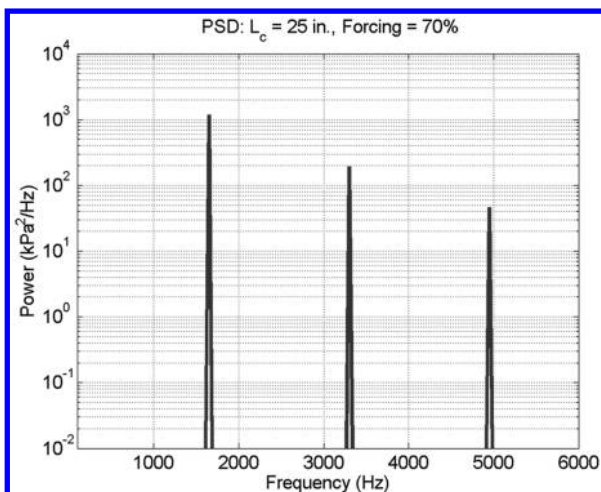

Fig. 16 FFT of nonlinear forcing results of test 25D1r showing excitation of the higher harmonics.

frequency ranges for the intermediate modes because precise values are difficult to discern. Further, classical acoustic estimates (without mean flow) are also included for comparison [20]. It is evident that the computed modes agree fairly well with the measured frequency values in all instances. As in the straight duct case, the zero-mean-flow acoustic estimates overpredict the correct frequencies.

As a further validation of the computational predictions, the computed mode shapes are compared with the experimental estimates of the chamber modes. The experimental estimates are determined by performing individual fast Fourier transforms (FFTs) at the various pressure transducer locations and then comparing the relative amplitudes of the dominant chamber modes in each case. The comparisons are shown for several test chamber lengths in Fig. 13. In each case, the dominant (i.e., unstable) mode is shown in the comparisons. It is clear that the computed mode shapes agree quite closely with the experimental values, particularly in the chamber, which is well instrumented. In most cases, experimental measurements at the injector head end also agree quite well with the predicted values in spite of differences in how the oxidizer inflow is modeled. In general, the close agreement confirms that the computational model faithfully represents the acoustic modes in the combined injector-combustor-nozzle configuration.

C. Nonlinear Forcing

We next assess the influence of nonlinear phenomena on the acoustic wave solutions in the longitudinal chamber configuration. To do this, we force the oxidizer flow rate by using specified frequencies as we did to determine the individual acoustic mode shapes; however, we now use larger forcing amplitudes to introduce nonlinear effects. Figure 14 shows typical results for test 25D1r and the second chamber mode (1650 Hz) using forcing amplitudes of 20 and 50%. These results are observed to be markedly different compared with the linear mode shapes obtained with 0.1% forcing (see Fig. 11). The mode shapes in Fig. 14 are observed becoming progressively more complicated even though the forcing function is a pure mode. In fact, the nonlinear modes are observed to have significantly higher harmonic content and there is clear evidence of wave steepening. Further, the sharp focusing of the pressure nodes is no longer present.

Figure 15 shows a comparison of the computed and measured pressure time histories for test 25D1r. The computational results are obtained by forcing the chamber at 1650 Hz, which corresponds to the dominant unstable frequency in the experiments. The results show a very good comparison of the wave-steepening effects at these nonlinear amplitudes. We note, however, that the computational results are forced by modulating the inlet oxidizer flow, whereas the experimental results are spontaneously unstable. We will present preliminary results with response function forcing in the following subsection.

The FFT of the nonlinear forcing results for test 25D1r are shown in Fig. 16. As expected, the FFT shows evidence of the higher harmonics of the 1650 Hz forcing frequency. We further note that this result compares qualitatively with the experimental results given in Fig. 4d for the 25-in. chamber. Indeed, the comparison confirms that the excitation of the higher modes is in fact due to the inherent nonlinearities of the high-amplitude oscillations observed in the tests.

D. Combustion Response

The computational results presented so far have involved external forcing of the oxidizer flow rate to stimulate the acoustics in the chamber. The prediction of combustion instability requires the inclusion of appropriate response functions that can naturally excite the instabilities. As a first step toward devising such models, we present results using the simple combustion response function described in Eq. (13). For purposes of the present demonstration, we set the time-lag term, $\tau = 0$, thereby ensuring that the response function satisfies Rayleigh's criterion. Different values of the normalized interaction index, n, are used to assess sensitivity to this parameter. In all the calculations shown here, the unsteady calculations are first initiated without the response function by using the discrete broadband forcing. Once the modes have been set up, the mass flux forcing is turned off and the combustion response function is turned on. The time histories are then analyzed and compared with the experimental data.

Figure 17 shows the time histories for two different values of the n parameter in the forcing function. For a small value of $n = 0.205$, the fluctuations are observed to be damped and the flowfield becomes stable. This damping is due to the presence of the exit boundary, which propagates the existing fluctuations out of the domain, and the response function is not strong enough to make the instabilities grow before they are washed out. On the other hand, for higher values of this parameter, such as $n = 2.05$, the growth rate due to the response function overwhelms the decay rate due to the outflow, and the fluctuations are seen to grow. This growth is initially linear and then it becomes strongly nonlinear before eventually reaching a limit cycle similar to the experimental results.

Figure 18 shows the Fourier transforms obtained by sampling several unstable cases, corresponding to the different experimental chamber length test cases. For definiteness, all cases employ the same simple combustion response model with an interaction index, $n = 2.05$. Although it cannot be claimed that the combustion response model is representative of the combustion instability mechanism in the experiments, it is nevertheless instructive to compare the predicted results with the experimental results shown in Fig. 4. Indeed, in many of the cases, the unstable frequency response is strikingly similar to the experimental results. For instance, the 10-in. chamber shows that the 2000 Hz frequency is unstable along with the related higher harmonic modes. Likewise, for the 25-in. chamber case, the dominant mode corresponds to the 1700 Hz mode and the associated harmonics. In the 35-in. case, the computational results correspond well with the experimental results in the later stages of the test, but not the early stages. Overall, we certainly cannot claim that the present simple response model will always select the correct mode. However, it does appear that the dominant modes in each case are particularly susceptible to instability. Importantly, our results demonstrate that the present computational platform can provide a very useful basis for the calibration and validation of more detailed combustion response models. In this regard, we reiterate the importance of obtaining reliable experimental data and note that additional experiments and diagnostics are in progress to facilitate such detailed analyses.
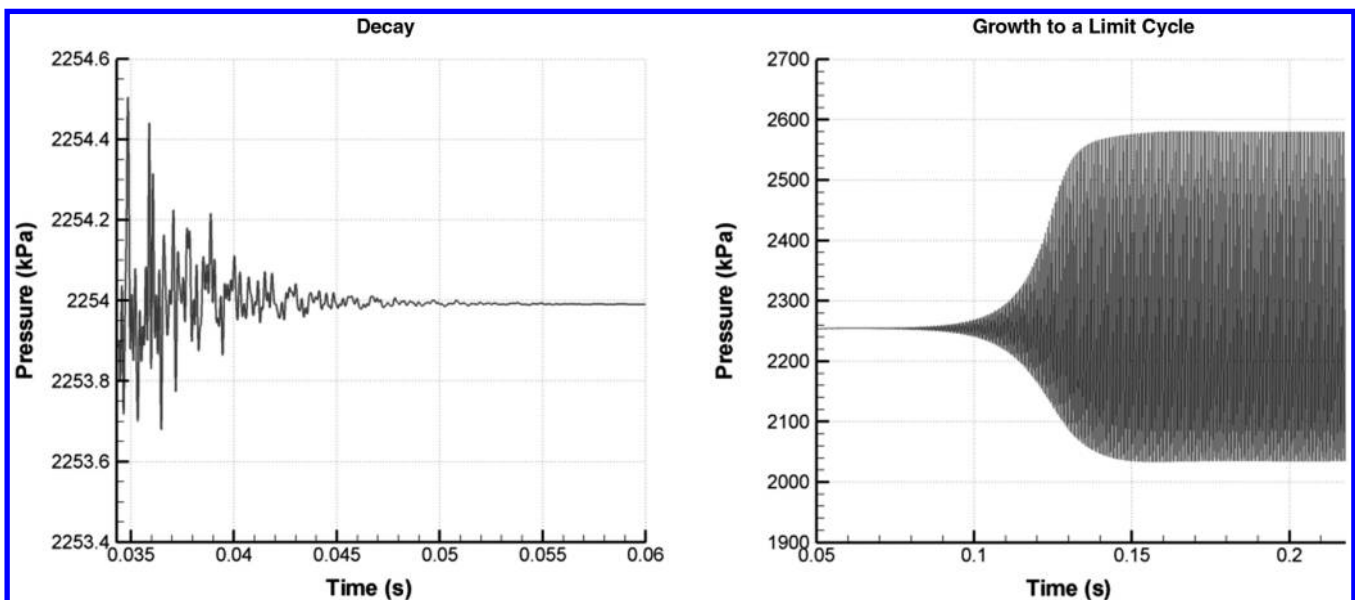

Fig. 17   Pressure time histories for two different β values in the response function definition: a) $n = 0.205$ shows decay, and b) $n = 2.05$ shows growth to a limit cycle.
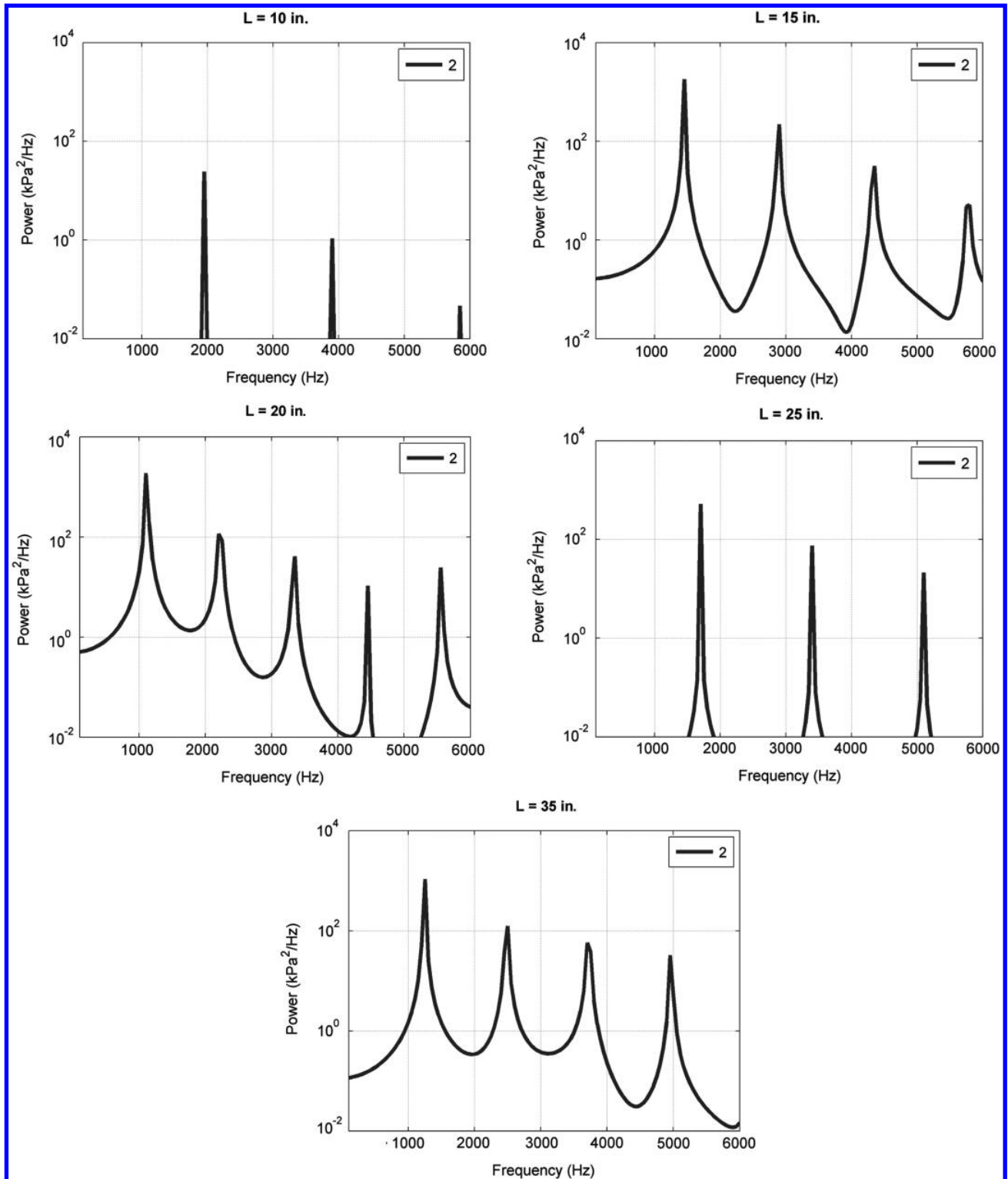
Fig. 18   FFTs of the computed unstable limit cycles for the 25- and 35-in. chamber test cases.

As a final comparison, we select the 25-in. case, for which the computed unstable mode matches the experimental mode, and compare the experimental and computational time histories at the different axial locations for which transducer data are available. The results are shown in Fig. 19. Superimposed on the time histories, the motion of the forward-running and backward-running waves is shown. Although these comparisons cannot be quantitative because of some subjectivity in the data interpretation, we note that there is very good qualitative agreement between the wave motion patterns in the experiments and computations. Based on these and the other comparisons shown in this paper, we may conclude that the present

approach is capable of correctly representing the flowfield in the experimental configuration. We are therefore confident that the computational model is a useful platform for the design, development, and calibration of combustion response functions, which can then be used in practical combustor design codes.

V.   Conclusions

Combustion instability in liquid rocket engines results from the complex interaction of multiphase effects, turbulence, combustion, and fluid dynamics with the chamber acoustics. Because of the
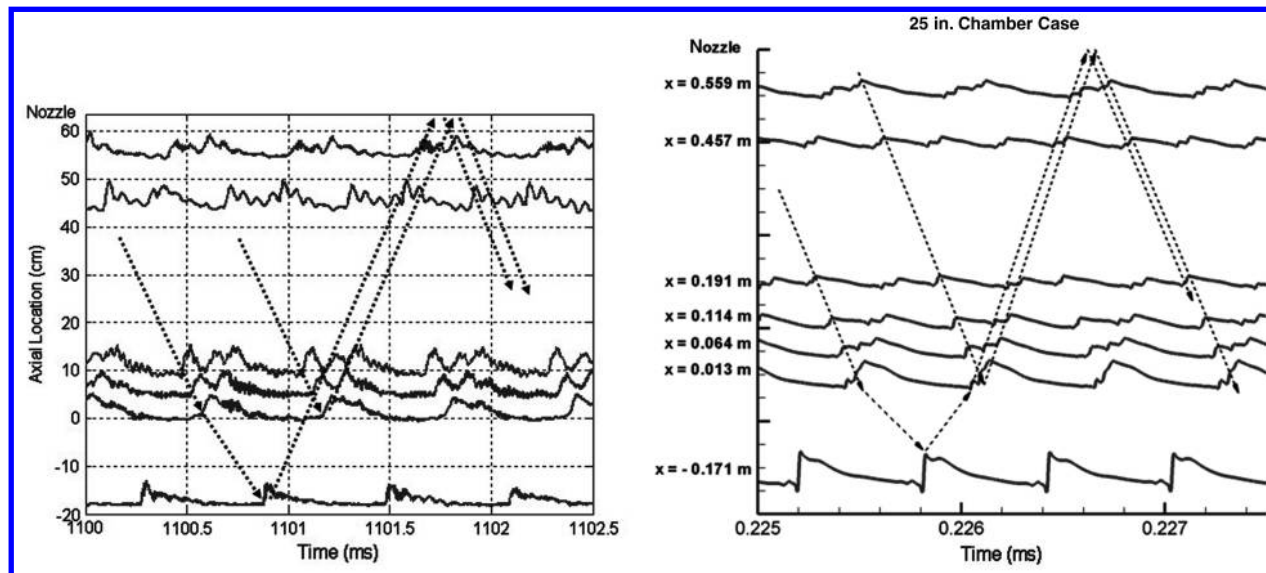
Fig. 19 Experimental measurements and computed predictions of pressure time histories at different axial locations for an unstable test condition.

physical modeling challenges of these interactions and the limitations in the availability of adequate computational resources, first-principles modeling of combustion instability remains beyond our current capabilities. It is therefore necessary to adopt combined experiments and computations as well as computational modeling at varying levels of fidelity to make progress in this difficult field. The present paper concerns the development of a computational model for studying combustion instability incidence in an experimental rocket chamber being tested at Purdue University. The overall idea is to use a detailed representation of the mean flowfield in the combustion chamber and appropriate combustion response functions for the unsteady dynamics in the injector and chamber. The long-term goal is to use the combined experimental–computational platform as a testbed to design and calibrate the response functions. The objective of the present paper is to carry out detailed validation of the acoustics and instability characteristics in the experimental longitudinal-mode combustor, which represents an important first step in reaching our eventual goal.

The computational model uses the full nonlinear Euler equations in quasi-one-dimensional form, which is appropriate for the longitudinal-mode experiments that are of interest here. Combustion is represented by a simple global mechanism involving fuel, oxidizer, and products. The unsteady computations are carried out by starting with a given mean-flow solution that corresponds to a given experimental test condition and then perturbing the inlet oxidizer flow with a combination of discrete frequencies. This approximates a "white noise" disturbance more effectively than a random frequency source. By controlling the amplitude of the forcing function, both linear and nonlinear effects may be assessed. Further, preliminary results using a simple combustion response function to represent spontaneously growing instabilities are also obtained. The basic computational model is also verified using standard acoustic solutions with mean-flow in a constant area duct. Additionally, these studies confirm the second-order accuracy of the computational method.

The computational model has been used to predict all the experimental test conditions. Linear forcing studies are used to determine the fundamental resonant frequencies of the single-injector-combustor configuration and to compare them with the classical acoustic estimates as well as the experimental estimates. In general, the current predictions agree well with the experimental data, whereas the classical zero-mean-flow acoustic frequencies are found to overpredict the frequencies in most cases. Comparisons of the predicted mode shapes agree very well with the corresponding experimental estimates, as do the predicted trends, due to changes in the chamber length and flow conditions. The nonlinear studies with the chamber being forced by a high-amplitude single discrete

frequency indicate that the higher harmonics are excited along with the wave-steepening effects. Both of these phenomena are also observed to correspond closely with the experimental observations.

These computational–experimental comparisons indicate that the computational model is capable of correctly representing the acoustic and instability characteristics in the longitudinal chamber. The computational framework can then be applied to test and calibrate appropriate combustion response functions. As a first step in this direction, we also present results using a simple pressure-coupled response function. Results indicate that, with the appropriate choice of the constants in such a model, spontaneously growing instabilities can be generated, leading to the expected limit cycles and other nonlinear phenomena. Although the present response function model is preliminary, we can conclude that the present methodology provides a sound basis for the development and calibration of more sophisticated versions of these models. This will be the subject of future research.

Acknowledgments

References

[1] Harrje, D. T., and Reardon, F. H. (eds.), "Liquid Propellant Rocket Combustion Instability," NASA SP-194, 1972.

[2] Yang, V., and Anderson, W. (eds.), *Liquid Rocket Engine Combustion Instability*, Vol. 169, Progress in Astronautics and Aeronautics, AIAA, Washington, D. C., 1995.

[3] Oefelein, J. C., and Yang, V., "Comprehensive Review of Liquid-Propellant Combustion Instabilities in F1 Engines," *Journal of Propulsion and Power*, Vol. 9, No. 5, Sept.–Oct. 1993, pp. 657–677.
doi:10.2514/3.23674

[4] Crocco, L., "The Sensitive Time Lag Theory," *Liquid Propellant Rocket Combustion Instability*, edited by D. T. Harrje, and F. H. Reardon, NASA, Washington, D. C., 1972; also NASA SP-194.

[5] Zinn, B. T., "A Theoretical Study of Nonlinear Combustion Instability in Liquid Propellant Engines," *AIAA Journal*, Vol. 6, No. 10, 1968, pp. 1966–1972.
doi:10.2514/3.4908

[6] Culick, F. E. C., "Combustion Instabilities in Liquid-Fueled Propulsion Systems: An Overview," AGARD CP-450, 1989.

[7] Yang, V., Wicker, J. M., and Yoon, M. W., " Acoustic Waves in

Combustion Chambers," *Liquid Rocket Engine Combustion Instability*, edited by V. Yang, and W. E. Anderson, AIAA, Washington, D. C., 1995, Chap. 13.

[8] Mitchell, C. E., "Analytical Models for Combustion Instability," *Liquid Rocket Engine Combustion Instability*, edited by V. Yang, and W. Anderson, Vol. 169, Progress in Astronautics and Aeronautics, AIAA, Washington, D. C., 1995, Chap. 15.

[9] Dowling, A. P., and Stow, R. S., "Acoustic Analysis of Gas Turbine Combustors," *Journal of Propulsion and Power*, Vol. 19, No. 5, 2003, pp. 751–763.
doi:10.2514/2.6192

[10] Suresh, M., and Jou, W., "Large-Eddy Simulations of Combustion Instability in an Axisymmetric Ramjet Combustor," *Combustion Science and Technology*, Vol. 75, Nos. 1–3, 1991, pp. 53–72.
doi:10.1080/00102209108924078

[11] Huang, Y., Wang, S., and Yang, V., "Systematic Analysis of Lean-Premixed Swirl-Stabilized Combustion," *AIAA Journal*, Vol. 44, No. 4, 2006, pp. 724–740.
doi:10.2514/1.15382

[12] Martin, C., Benoit, L., Sommerer, Y., Nicoud, F., and Poinsot, T., "Large Eddy Simulation and Acoustic Analysis of a Swirl-Staged Turbulent Combustor," *AIAA Journal*, Vol. 44, No. 4, 2006, pp. 741–750.
doi:10.2514/1.14689

[13] Rey, C., Ducruix, D., and Candel, S., "A Method for the Transverse Modulation of Reactive Flows with Application to Combustion Instability," *Combustion Theory and Modeling*, Vol. 9, No. 1, 2005, pp. 5–22.
doi:10.1080/13647830500051950

[14] Grenda, J. M., Sankaran, V., and Merkle, C. L., "Application of Computational Fluid Dynamics Techniques to Engine Instability Studies," *Liquid Rocket Engine Combustion Instability*, edited by V. Yang, and W. Anderson, Vol. 169, Progress in Astronautics and Aeronautics, AIAA, Washington, D. C., 1995, Chap. 19.

[15] Habiballah, M., and Dubois, I., "Numerical Analysis of Engine Instability," *Liquid Rocket Engine Combustion Instability*, V. Yang, and W. Anderson, Vol. 169, Progress in Astronautics and Aeronautics, AIAA, Washington, D. C., 1995, Chap. 18.

[16] Longatte, E., Lafon, P., and Candel, S., "Computational of Acoustic Propagation in Two-Dimensional Sheared Ducted Flows," *AIAA Journal*, Vol. 38, No. 3, March 2000, pp. 389–394.
doi:10.2514/2.992

[17] Miller, K. J., Nugent, N., Sisco, J., and Anderson, W., "Experimental Study of Combustion Instabilities In a Single-Element Coaxial Swirl Injector," *Journal of Propulsion and Power*, Vol. 23, No. 5, 2007, pp. 1102–1112.

[18] Sisco, J. C., Smith, R. J., Nugent, N. J., Sankaran, V., and Anderson, W. E., "Examination of Mode Shapes in an Unstable Model Rocket Combustor," AIAA Paper 2006-4525, 2006.

[19] Marshall, W., Woodward, R., Pal, S., Santoro, R., Smith, R., Xia, G., Sankaran, V., and Merkle, C. L., "Experimental and Computational Investigation of Combustor Acoustics and Instabilities, Part II: Transverse Modes," AIAA 2006-0538, 2006.

[20] Smith, R., Nugent, N., Sisco, J., Xia, G., Anderson, W., Sankaran, V., and Merkle, C. L., "Experimental and Computational Investigation of Combustor Acoustics and Instabilities Part I: Longitudinal Modes," AIAA 2006-0537, 2006.

[21] Li, D., Sankaran, V., Lindau , J., and Merkle, C. L., "A Unified Formulation for Multi-Component and Multi-Phase Flows," AIAA Paper 2005-1391, 2005.

[22] McBride, B. J., Zehe, M. J., and Gordon, S., "NASA Glenn Coefficients for Calculating Thermodynamic Properties of Individual Species," NASA TP-2002-211556, 2002.

[23] Smith, R. J., "Computational Modeling of High-Frequency Combustion Instability in a Single-Element Liquid Rocket Engine," M.S. Thesis, Purdue University, West Lafayette, IN, Aug. 2006.

C. Bailly
Associate Editor

This article has been cited by:

1. Brian Pomeroy, William Anderson. Transverse Instability Studies in a Subscale Chamber. *Journal of Propulsion and Power*, ahead of print1-9. [Abstract] [Full Text] [PDF] [PDF Plus]

2. Cheng Huang, William E. Anderson, Charles MerkleExploration of POD-Galerkin Techniques for Developing Reduced Order Models of the Euler Equations . [Citation] [PDF] [PDF Plus]

3. Emanuele Martelli, Barbara Betti, Francesco NasutiSeparation Shock Cutoff Frequency in Dual Bell Nozzles . [Citation] [PDF] [PDF Plus]

4. Cheng Huang, William E. Anderson, Charles MerkleGlobal POD-Based Adaption Scheme for Reduced Order Models of the Reaction-Advection Equation . [Citation] [PDF] [PDF Plus]

5. Matthew K. Wierman, William Z. Hallum, William E. Anderson, Benjamin L. AustinOxidizer Post Resonance Response of a High Pressure Combustor . [Citation] [PDF] [PDF Plus]

6. Maria Luisa Frezzotti, Francesco Nasuti, Cheng Huang, Charles Merkle, William E. AndersonResponse Function Modeling in the Study of Longitudinal Combustion Instability by a Quasi-1D Eulerian Solver . [Citation] [PDF] [PDF Plus]

7. Maria Luisa Frezzotti, Francesco Nasuti, Cheng Huang, Charles Merkle, William E. AndersonDetermination of Heat Release Response Function from 2D Hybrid RANS-LES Data for the CVRC Combustor . [Citation] [PDF] [PDF Plus]

8. Matthew K. Wierman, W. Zach Hallum, William E. AndersonStability Characterization of a High Pressure Transverse Combustor with Discretely Variable Oxidizer Post Lengths . [Citation] [PDF] [PDF Plus]

9. Maria L. Frezzotti, Andrea Terracciano, Francesco Nasuti, Sarah Hester, William E. AndersonLow-order model studies of combustion instabilities in a DVRC combustor . [Citation] [PDF] [PDF Plus]

10. Cheng Huang, William E. Anderson, Charles MerkleExploration of POD-Galerkin Method in Developing a Flame Model for Combustion Instability Problems . [Citation] [PDF] [PDF Plus]

11. Charles T. Haddad, Joseph Majdalani. 2013. Transverse Waves in Simulated Liquid Rocket Engines. *AIAA Journal* 51:3, 591-605. [Abstract] [Full Text] [PDF] [PDF Plus]

12. Yen Yu, James C. Sisco, Stanford Rosen, Ajay Madhav, William E. Anderson. 2012. Spontaneous Longitudinal Combustion Instability in a Continuously-Variable Resonance Combustor. *Journal of Propulsion and Power* 28:5, 876-887. [Citation] [PDF] [PDF Plus]

13. Thomas Feldman, Matthew Harvazinski, Charles Merkle, William AndersonComparison Between Simulation and Measurement of Self-Excited Combustion Instability . [Citation] [PDF] [PDF Plus]

14. Charles Haddad, Joseph MajdalaniTransverse Waves in Simulated Liquid Rocket Engines . [Citation] [PDF] [PDF Plus]

15. G. Xia, M. Harvazinski, W. Anderson, C. MerkleInvestigation of Modeling and Physical Parameters on Instability Prediction in a Model Rocket Combustor . [Citation] [PDF] [PDF Plus]

16. Brian Pomeroy, Collin Morgan, William AndersonResponse of a Gas-Centered Swirl Coaxial Injector to Transverse Instabilities . [Citation] [PDF] [PDF Plus]

17. Stanford Rosen, Mark Pfeil, Yen Yu, William AndersonEffects of Hydrogen Addition on Combustion Stability of an Unstable Methane Rocket Combustor . [Citation] [PDF] [PDF Plus]

18. R. Smith, G. Xia, W. A. Anderson, C. L. Merkle. 2010. Computational Simulations of the Effect of Backstep Height on Nonpremixed Combustion Instability. *AIAA Journal* 48:9, 1857-1868. [Citation] [PDF] [PDF Plus]

19. Brian Pomeroy, Nicholas Nugent, William AndersonMeasuring Transverse Stability Combustion Response at Full Scale Frequencies in a Subscale Combustor . [Citation] [PDF] [PDF Plus]

20. Y. C. Yu, J. C. Sisco, V. Sankaran, W. E. Anderson. 2010. Effects of Mean Flow, Entropy Waves, and Boundary Conditions on Longitudinal Combustion Instability. *Combustion Science and Technology* 182, 739-776. [CrossRef]

21. Seong-Ku Kim, Hwan-Seok Choi, Dong-Jin Cha. 2010. Development of Helmholtz Solver for Thermo-Acoustic Instability within Combustion Devices. *Journal of the Korean Society for Aeronautical Space Science* 38, 445-455. [CrossRef]

22. Brian Pomeroy, Warren Lamont, William AndersonSubscale Tool for Determining Transverse Combustion Response . [Citation] [PDF] [PDF Plus]

23. Yen Yu, Loral O'Hara, James Sisco, William AndersonExperimental Study of High-Frequency Combustion Instability in a Continuously Variable Resonance Combustor (CVRC) . [Citation] [PDF] [PDF Plus]